# On the Systematic Long-Period Noise Reduction on Ocean Floor Broadband Seismic Sensors Collocated with Differential Pressure Gauges

by Taka'aki Taira, Zhao Zheng, and Barbara Romanowicz[*]

**Abstract** Vertical-component broadband seismic data collected on the ocean floor at regional distances from the shore and water depths on the order of 1–2 km are polluted by noise due to ocean infragravity (IG) waves in a period range (20–200 s) that is critical for regional structure studies and the determination of moment tensors for regional earthquakes. Using broadband seismic and differential pressure gauge data collected at the Monterey Ocean Bottom Broadband (MOBB) observatory, which has been operational since 2002, we identify the optimal length of time window to obtain the transfer function between the vertical seismic and pressure records. The maximum reduction in IG-wave-induced noise is obtained by using a one-day stack of transfer function inferred from data segment collected in the last 24 hours prior to data in which the noise removal method is applied. We show that a one-year stack of transfer function effectively reduces the noise level in the period band 50–100 s by 20 dB and by up to 15 dB at shorter periods. This resultant 20 dB noise reduction is comparable to that obtained from the one-day stack of transfer function. Our result suggests that the removal of noise induced by IG waves on MOBB vertical-component data can be done routinely without continuously calibrating the transfer function, also in near-real time, and is therefore also useful for routine regional moment tensor determination. This noise removal method has been implemented in the moment tensor determination system of the Northern California Seismic System.

## Introduction

Vertical-component data from broadband stations installed on the ocean floor at regional distances from the coast exhibit increased noise levels, compared to land stations, at long periods (typically 20–200 s), due to the effect of ocean infragravity (IG) waves induced by a dynamic ocean environment. This period range is essential for several applications: structural studies using surface waves as well as moment tensor inversion of regional earthquakes. In particular, rapid moment tensor determination of regional earthquakes is one of the crucial components in real-time earthquake hazard assessment in regions such as California (Sipkin, 1982; Dreger and Helmberger, 1991; Romanowicz et al., 1993; Dreger and Romanowicz, 1994; Pasyanos et al., 1996; Tajima et al., 2002; Ichinose et al., 2003; Clinton et al., 2006; Guilhem and Dreger, 2011). This is also the period range of choice for studies of regional structure using surface waves. Surface-wave observations from offshore stations are necessary to constrain structural transitions in the crust and upper mantle at the edges of continents.

In practice, the reliability of the moment tensor determination strongly depends on the station azimuthal coverage (e.g., Ford et al., 2010). Improved estimates of the moment tensor could be achieved by integrating broadband seismic data from ocean-bottom seismographs (OBSs) in near-coastal regions and on the seaside of offshore active faults, for which OBS data fill the gap of station azimuthal coverage. Minimizing IG-wave-induced signals on broadband OBS records is therefore essential. In particular, developing an automatic procedure for IG-wave-induced signal removal is crucial to make use of OBS records for real-time moment tensor determination.

Long-term data collection at the Monterey Ocean Bottom Broadband (MOBB) observatory (Romanowicz et al., 2003, 2006) offers a unique opportunity to characterize IG-wave-induced signals on OBS records and to develop an optimal near-real-time procedure for their removal. Additionally, station MOBB is the only offshore broadband seismic station in central California (Fig. 1), except for the

*Also at Collège de France, 11 Place Marcelin Berthelot, 75005 Paris, France.
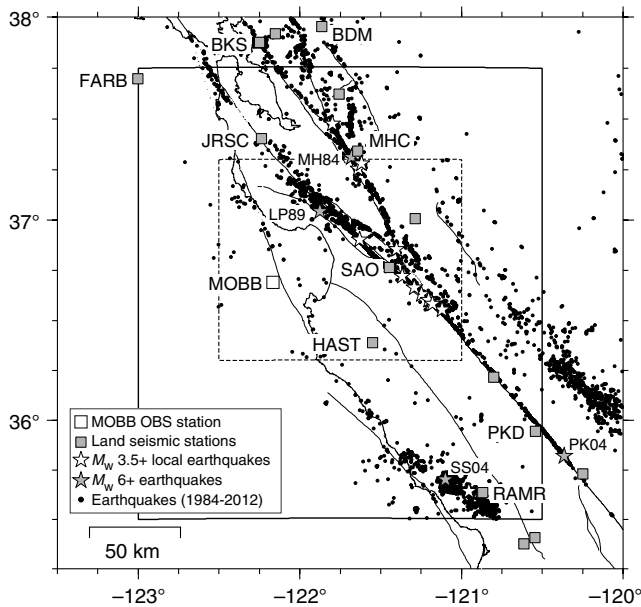
**Figure 1.** Map view of the ocean-bottom MOBB station with land-based broadband stations. The solid and dashed line rectangles are the target areas (see text for details) to identify the 12 $M_w \geq 3.5$ local earthquakes analyzed in this study. Also shown are earthquakes during 1984–2012 (Waldhauser and Schaff, 2008; see Data and Resources), the surface fault traces (thin lines; see Data and Resources) and the locations of $M_w$ 6+ historical earthquakes (MH84, the 1984 $M_w$ 6.2 Morgan Hill earthquake; LP89, the 1989 $M_w$ 6.9 Loma Prieta earthquake; SS04, the 2004 $M_w$ 6.5 San Simeon earthquake; and PK04, the 2004 $M_w$ 6.0 Parkfield earthquake).

island-based Farallon Islands station (station FARB) of the Berkeley Digital Seismic Network (BDSN; Romanowicz *et al.*, 1993). It thus provides complementary azimuthal coverage of the San Andreas fault system to the land-based network. Moreover and most importantly, broadband OBS data from station MOBB have now been available in real time since February 2009 (Romanowicz *et al.*, 2009).

## Data and Methodology

### MOBB Observatory

Station MOBB was installed in April 2002, at a water depth of 1000 m about 40 km offshore in Monterey Bay, California, (Fig. 1) through a collaborative effort between the Monterey Bay Aquarium Research Institute (MBARI) and the Berkeley Seismological Laboratory (BSL). Station MOBB is equipped with three geophysical sensors: (1) a three-component broadband Güralp CMG-1T seismometer, with corners at periods of 0.02 and 360 s, (2) a differential pressure gauge (DPG; Cox *et al.*, 1984), and (3) an ocean-bottom current meter. Broadband seismic data are sampled at 20 Hz while DPG and ocean-bottom current data are sampled at 1 Hz (Romanowicz *et al.*, 2003, 2006). The seismometer package is installed inside a Polyvinyl-chloride cylinder that was buried in the seafloor, and covered with glass beads (Romanowicz *et al.*, 2003). This was

performed with the help of the MBARI remotely operated underwater vehicle "Ventana".

After seven years of autonomous operation, in February 2009, the MOBB instrument package was successfully connected to the Monterey Accelerated Research System (MARS) fiber-optic cable, and the data have been available in real time at the Northern California Earthquake Data Center (Romanowicz *et al.*, 2009; see Data and Resources). Since then, the data completeness has significantly improved, and the internal clock drift of the MOBB seismic sensor has been continuously monitored (D. Neuhauser, personal comm., 2012).

## Observation of IG Waves

IG waves are primarily generated by nonlinear interactions between short-period ocean waves with periods of 5–20 s along the nearshore region (Munk, 1949; Tucker, 1950; Sutton *et al.*, 1965; Snodgrass *et al.*, 1966; Herbers *et al.*, 1995). Seafloor deformation under the pressure forcing by IG waves results in long-period seismic signals (20–500 s) on OBS records (e.g., Webb *et al.*, 1991; Webb, 1998; Dolenc *et al.*, 2005; Laske *et al.*, 2009; Bromirski *et al.*, 2010; Yang *et al.*, 2012). At station MOBB, seismic signals induced by IG waves are generally more dominant on the vertical component than on horizontal components (Dolenc *et al.*, 2005).

We compared the background noise level of the MOBB vertical-component data, with those from other stations installed on land (Fig. 2). Because of the IG-wave-induced seismic signals, the background noise level of station MOBB shows a marked increase in the period range 20–200 s, compared with those from land stations. In the period range 1–10 s, increased noise levels observed at all stations correspond to the double-frequency microseismic peak. A smaller peak at a period of 12 s corresponds to single-frequency microseisms.

The 20–200 s period band for the IG-wave-induced signals generally overlaps with that used for a variety of seismic analyses including surface-wave imaging studies (e.g., Ritzwoller *et al.*, 2002; Pasyanos, 2005; Obrebski *et al.*, 2011) and seismic moment tensor analysis for regional earthquakes (e.g., Dreger and Romanowicz, 1994; Kao *et al.*, 1998; Kubo *et al.*, 2002; Stich *et al.*, 2003; Bernardi *et al.*, 2004; Brandt and Saunders, 2011).

During stormy weather, the IG-wave-induced signal is observed in a broader period range (∼20–500 s) and its amplitude is higher (Fig. 2b). As only the energy of IG waves with wavelengths longer than the water depth is coupled with ocean floor, the IG-wave-induced signals are not observed at periods shorter than 20 s at station MOBB. This is the hydrodynamic effect, resulting in a "low-noise notch" (between the microseismic and the IG-wave peak), the width of which varies with the depth of water (Araki *et al.*, 2004; Dolenc *et al.*, 2008; Laske *et al.*, 2009; Webb and Crawford, 2010; Bécel *et al.*, 2011; Yang *et al.*, 2012). As shown in Dolenc *et al.* (2005), because of the depth of water of 1000 m at station MOBB, this low-noise notch is limited to the period

(a)



(b)
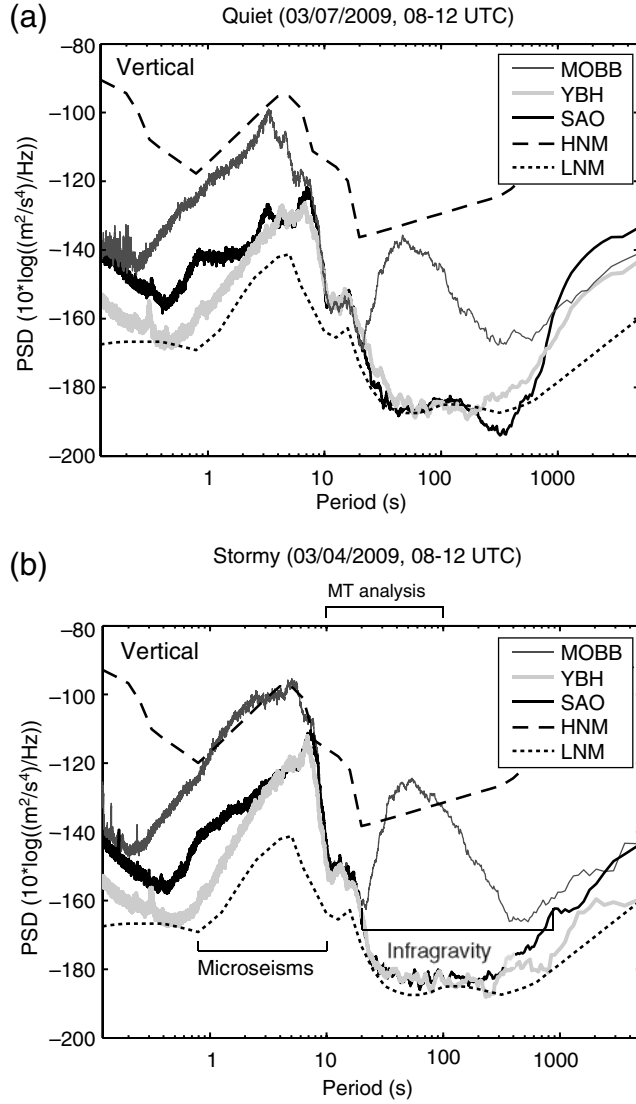


**Figure 2.** Power spectral densities (PSDs) of 4 hour long noise data in the vertical component recorded at ocean-bottom station MOBB and two other BSDN land stations SAO and YBH (one of the quietest stations of the BDSN, located 560 km north of station MOBB) on two days in 2009 when no significant earthquake signals were recorded. The top and bottom panel show PSDs obtained on (a) a "quiet day" and (b) a "stormy day", respectively. Also shown are the U.S. Geological Survey high- (HNM) and low-noise (LNM) models (Peterson, 1993). Increased noise levels for periods 20–200 s (induced by IG waves) are observed at station MOBB on both quiet and stormy days. A period range 10–100 s is used for our moment tensor analysis.

range 10–20 s, in which the background noise level of MOBB data is comparable to that of land stations (Fig. 2).

### Removal of IG-Wave Induced Signal on Vertical-Component OBS Data

Following previous studies (e.g., Webb and Crawford, 1999; Crawford and Webb, 2000; Crawford *et al.*, 2006; Dolenc *et al.*, 2007), the noise removal method we have em-

ployed makes use of the frequency-dependent transfer function between vertical seismic and pressure recordings to predict the deformation signal induced by IG waves on the vertical component. Ambient noise on DPG records is primarily induced by IG waves (Webb and Crawford, 1999). The transfer function allows the removal of the predicted deformation signal induced by IG waves from the vertical seismic records.

In the frequency domain, the transfer function, $T(\omega)$, at frequency $\omega$, can be expressed as

$$T(\omega) = \gamma(\omega) \sqrt{G_{ss}(\omega)/G_{pp}(\omega)}, \quad (1)$$

in which $G_{ss}(\omega)$ and $G_{pp}(\omega)$ are the average ensembles of one-sided auto-spectral density functions for vertical component and pressure records, respectively, and $\gamma(\omega)$ is the coherence between these records (Webb and Crawford, 1999). We used the coherence function defined by Bendat and Piersol (1986) as

$$\gamma(\omega) = \frac{G_{sp}(\omega)}{[G_{ss}(\omega)G_{pp}(w)]^{1/2}}, \quad (2)$$

in which $G_{sp}(\omega)$ is the average ensemble of one-sided cross-spectral density functions between vertical component and pressure records. Following Crawford and Webb (2000), we estimate $G_{ss}(\omega)$, $G_{pp}(\omega)$, and $G_{sp}(\omega)$ from the Fourier transforms of the observed vertical-component data $S(\omega)$ and pressure recordings $P(\omega)$:

$$G_{ss}(\omega) = \left(\frac{2}{NL}\right) \sum_{i=1}^{N} |S_i(\omega)|^2,$$

$$G_{pp}(\omega) = \left(\frac{2}{NL}\right) \sum_{i=1}^{N} |P_i(\omega)|^2, \quad \text{and}$$

$$G_{sp}(\omega) = \left(\frac{2}{NL}\right) \sum_{i=1}^{N} S_i^*(\omega)P_i(\omega), \quad (3)$$

in which $S_i(\omega)$ and $P_i(\omega)$ are the Fourier transforms of the vertical component and pressure records, respectively for the data window $i$, and $N$ and $L$ are the number of data windows and the length of data window, respectively. The asterisk represents the complex conjugate.

The coherent part of the pressure record corresponding to IG-wave-induced signals is subtracted from the vertical-component seismogram, and the resulting spectrum of the vertical-component seismogram after correction for IG-wave-induced signal $S'(\omega)$ can be expressed as

$$S'(\omega) = S(\omega) - T^*(\omega)P(\omega). \quad (4)$$

The noise removal of IG-wave-induced signals with the transfer function is based on the high temporal correlation ($\gamma(\omega)$ in equation 2) between the vertical component and DPG records in the IG waveband. This temporal correlation between MOBB OBS and DPG data is examined in the Temporal Behavior of Transfer Function section.
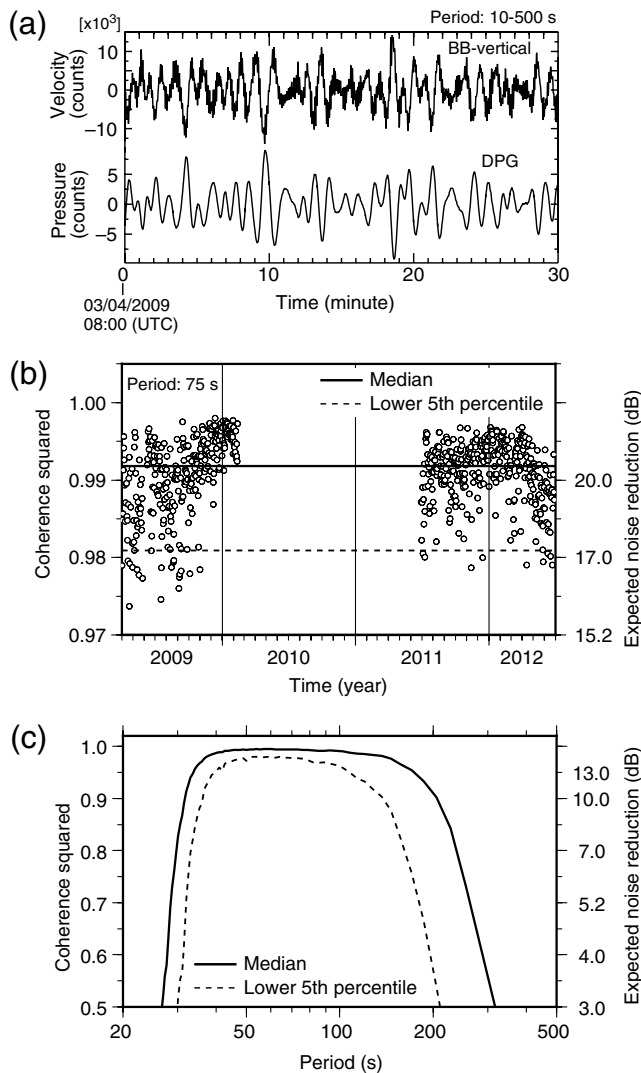
**Figure 3.** Correlation between the vertical component of seafloor ground velocity and the water pressure inferred from the DPG record in the IG waveband. (a) Observed 30 minute long MOBB vertical-component data (the top trace) and DPG record (the bottom trace) with a 10–500 s band-pass filter. (b) Temporal behavior of the coherence squared between MOBB vertical component and DPG records at a period of 75 s. The solid line is the median coherence squared (0.9918). The dashed line is the lower fifth percentile (0.9809) obtained from the coherence-squared distribution estimated by analyzing 4487 3 hour long records. Note that the MOBB data were not available during April 2010 through June 2011. (c) The median coherence squared (the solid line) and the lower fifth percentile of the coherence-squared distribution as a function of period. Also shown in Figure 3b,c is the theoretical limit of noise reduction (the right axis) introduced by Webb and Crawford (1999), inferred from the coherence squared (see text for details).

## Results and Discussion

### Temporal Behavior of Transfer Function

We have systematically analyzed all available MOBB broadband seismic and DPG records collected between February 2009 and June 2012 and computed the transfer function between them as described above (equation 1). Prior to February 2009, that is, when MOBB was an autonomous station, visited every 3–4 months, data analysis is made more difficult due in particular to the presence of time offsets between the broadband seismic and DPG channels caused by internal clock drifts of the seismometer. Note that the cable which links the MOBB instrumentation to the MARS science node was trawled in February 2010, and about a year of data is missing, until it was possible to replace the cable in June 2011.

As previously noted (Dolenc *et al.*, 2007), in the absence of earthquakes, vertical displacement and pressure records are nearly perfectly coherent in the IG waveband (Fig. 3a). The continuous MOBB OBS and DPG records are split into nonoverlapping 3 hour long segments, to examine the temporal behavior of the coherence and the transfer function. In each single 3 hour long data, we employed a moving-window cross-correlation analysis by using a 2048 s time window with 50% overlap to compute the ensemble averaged cross-correlation spectra. The use of this short-time window with overlap will minimize effects of long-duration wavetrains from teleseismic earthquakes in the coherence and transfer function estimates.

We examined the variability of the coherence squared, by computing the median and the lower fifth percentile of the coherence-squared distribution obtained from the 3 hour long data set (Fig. 3b). We used the lower fifth percentile as the lower bound of the coherence squared. We obtained 4487 3 hour long records used to estimate the distribution of the coherence squared. For example, at a period of 75 s, the median and the lowest 5% of the coherence squared are 0.9918 and 0.9809, respectively.

Our measurement shows the median values of the coherence squared in the period band 30–200 s are higher than 0.990 (Fig. 3c) which corresponds to the theoretical limit of noise reduction of about 20 dB inferred from $10 \times \log_{10}[1 - \gamma^2(\omega)]$ introduced in Webb and Crawford (1999). The high median coherence squared ($> 0.990$) in the period band 30–200 s indicates that the seismic signals observed on the vertical component, in the absence of earthquakes, are primarily due to seafloor deformation under pressure loading induced by IG waves. Therefore, deformation signals computed with the transfer function ($T^*(\omega) \times P(\omega)$ in equation 4) represent the IG-wave-induced signals on the MOBB vertical-component data well. The lower fifth percentile of the coherence-squared distribution, however, shows rapid decays of the coherence squared below 40 s and above 100 s (Fig. 3c). The amount of noise reduced by the transfer function will thus vary for individual 3 hour long segments analyzed.

We observe several excursions in the transfer function associated with the internal clock drifts and timing corrections of the MOBB OBS (Fig. 4). We manually excluded this type of excursions from our data sets based on the station MOBB log file (D. Neuhauser, personal comm., 2012). This procedure rejects 16% of the 3 hour long data and the total
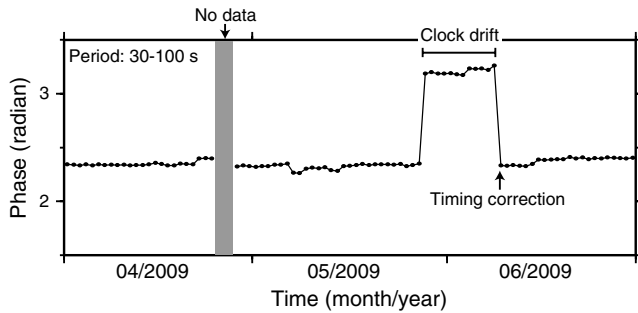
**Figure 4.** Temporal behavior of the phase response of the transfer function averaged over the period range 30–100 s for a 3 month period (April through June 2009). A change of the phase response occurred during 22 May through 9 June 2009 because of an internal clock drift of the MOBB OBS sensor. The transfer functions obtained during this period were excluded in the computation of the median transfer functions shown in Figures 5 and 6. The resultant transfer functions shown here are one-day moving averages.

number of the 3 hour long segments used in this study is 4487.

The temporal evolution of the transfer function shows an abrupt change in transfer function from the 3 hour long segment between March 2010 and July 2011, that is, at both ends of the interruption due to the cable failure (Fig. 5). This change corresponds to the replacement of the DPG by another sensor of the same type, with nominally the same instrument response function, while the seismometer was not modified (P. McGill, personal comm., 2012). The replacement of the DPG appears to introduce a constant offset in the transfer function (Fig. 5b,d). Our observation illustrates that different DPGs actually have significantly different instrument responses, which may be important for certain types of studies relying on the DPG calibrations (e.g., Baba *et al.*,

2004; Saito *et al.*, 2010, 2011; Ito *et al.*, 2011; Maeda *et al.*, 2011).

As shown in Figure 5a, there appears to be a seasonal variation in the amplitude response of the transfer function at a period of 25 s during the time interval April 2009 to February 2010. The amplitude response at this period systematically increases by a factor of about 2 from northern hemisphere summer (April through September 2009) to winter (October through December 2009 and January through February 2010). One possible explanation for this systematic change is that it is due to a temperature effect (Barzilai *et al.*, 1998). A systematic temporal variation is not observed during the time interval July 2011 to June 2012 although the variability of the amplitude of the transfer function is comparable to that observed during the time interval April 2009 to February 2010. To characterize the temporal variations of the transfer function at a period of 25 s and the possible causes of the fluctuations will require analyzing longer term data sets and will be addressed in a further study.

We obtained the one-day stacks of transfer function and examined their variability (Fig. 6). We determined that a one-day time window is the optimal window length to compute the transfer function in order to obtain the maximum reduction in the IG-wave-induced signals on the vertical-component data (see the Obtaining Improved Vertical Waveform Data section). Similarly to the estimate of the coherence squared, we estimated the median amplitude and phase responses for the one-day stack of transfer function, and the lower and higher fifth percentiles, from the distributions of the amplitude and phase responses, to address the variability of the transfer function (Fig. 6). Because of the abrupt change in the transfer function related to the replacement of DPG that occurred in July 2011, we used the two time intervals, before and after the DPG
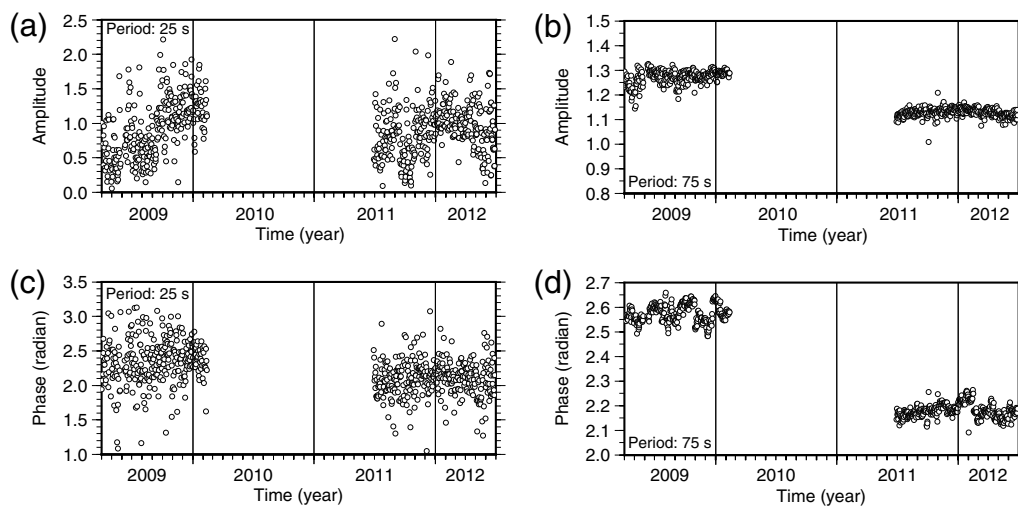


**Figure 5.** Temporal variations in transfer function at periods of 25 and 75 s. (a, b) Amplitude and (c, d) phase responses of one-day stacks of transfer function obtained from 3 hour long data. The transfer functions obtained at a period of 25 s are shown in Figure 5a,c while those functions obtained at a period of 75 s are shown in Figure 5b,d. Note that the MOBB data were not available during April 2010 through June 2011.
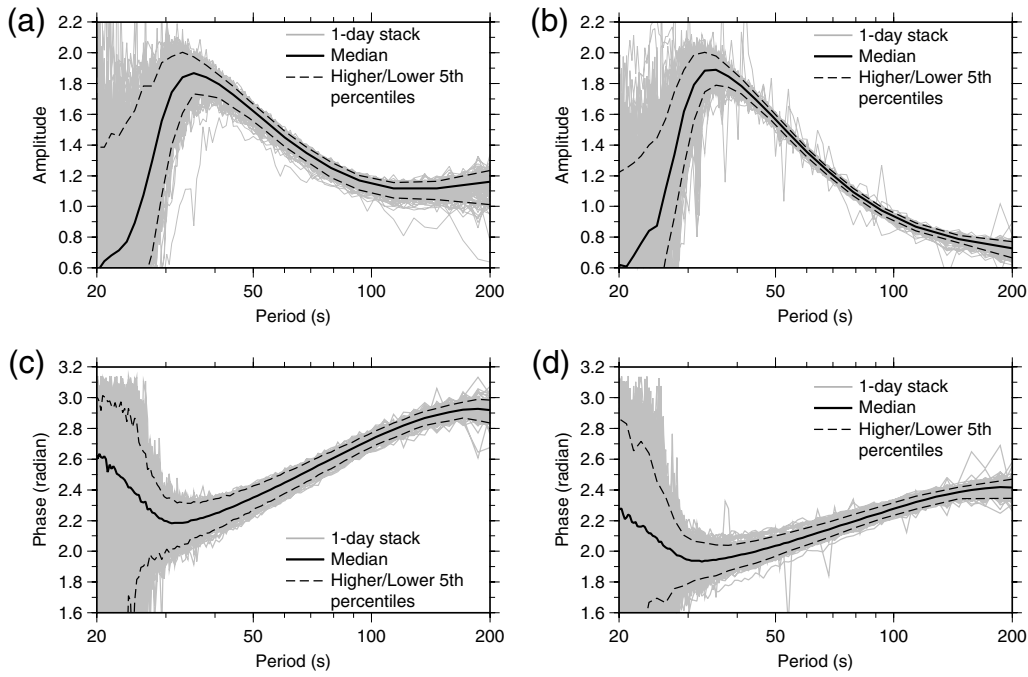
**Figure 6.** Variabilities of one-day stacks of transfer functions in time intervals 2009–2010 and 2011–2012. (a, b) Amplitude and (c, d) phases responses of one-day stacks of transfer function. The solid lines are the median values (the solid line). The transfer functions obtained in the time interval 2009–2010 are shown in Figure 6a,c while those functions obtained in the time interval 2011–2012 are shown in Figure 6b,d. Also shown are the lower and higher fifth percentiles (the dashed lines) of the distribution of the transfer functions.

replacement to estimate the variability of the one-day stack of transfer function.

The two reference transfer functions are obtained by applying a median stacking of transfer functions (the solid lines in Fig. 6). These two reference transfer functions computed from the 2009–2010 and the 2011–2012 data hereafter are referred to as tf2009 and tf2011, respectively. As the lower and upper bounds of the one-day stack of transfer function, we computed the lower and higher fifth percentiles from the distribution of the one-day stacks of transfer function (the dashed lines in Fig. 6). In each case, we estimated the percentage difference between the one-day stacks of the transfer function and the reference transfer function $\{[A_d(\omega) - A_r(\omega)]/A_r(\omega)\} \times 100(\%)$ and $\{[\phi_d(\omega) - \phi_r(\omega)]/\phi_r(\omega)\} \times 100(\%)$, in which $A(\omega)$ and $\phi(\omega)$ are the amplitude and phase responses, respectively, and the subscripts d and r indicate the one-day stack of transfer function and the reference transfer function.

Our analysis indicates that the amplitude and phase responses in the period band 50–100 s vary within the ranges of −5.6%–2.8% and −3.1%–3.4%, respectively. In the wider-period range 35–200 s, the variabilities of the amplitude and phase responses are −10.68%–5.64% and −5.01%–6.11%, respectively.

### Obtaining Improved Vertical Waveform Data

We obtained the MOBB vertical-component data with reduced IG-wave-induced noise, by applying the two refer-

ence transfer functions, tf2009 and tf2011 (Fig. 7a). We used tf2009 and tf2011 for data collected in the time intervals 2009–2010 and 2011–2012, respectively. To estimate the variability of the noise reduction obtained with the reference transfer functions, we evaluated the median and lower fifth percentile from the distribution of noise reductions obtained from individual 3 hour long data as a function of period (Fig. 7b).

By using the reference transfer functions, the resulting median noise reduction in the period range 50–100 s is about 20 dB, which is comparable to the theoretical maximum reduction in the noise level inferred from the coherence squared (Fig. 3c). In this period range, the lower fifth percentile of the distribution of noise reduction ranges from 13 to 15 dB. This suggests that using a one-year stack of transfer function reduces the noise level on the MOBB vertical-component data by at least 13–15 dB for any time window in the period band 50–100 s. At shorter periods, the amount of noise reduction is lower. We are however able to obtain a 5–15 dB noise reduction at periods greater than 30 s, which is important for our moment tensor analysis.

We additionally examined the amount of noise reduction by applying a set of transfer functions with different time windows, in order to identify the optimal length of time window to minimize the IG-wave-induced noise on the vertical-component data. In addition to the reference transfer functions, tf2009 and tf2011, we computed four different transfer functions with time windows of (1) 3 hours, (2) 1 day, (3) 10 days, and (4) 50 days. Those four transfer

(a)

01/19/2010, 00-03 UTC



(b)



(c)
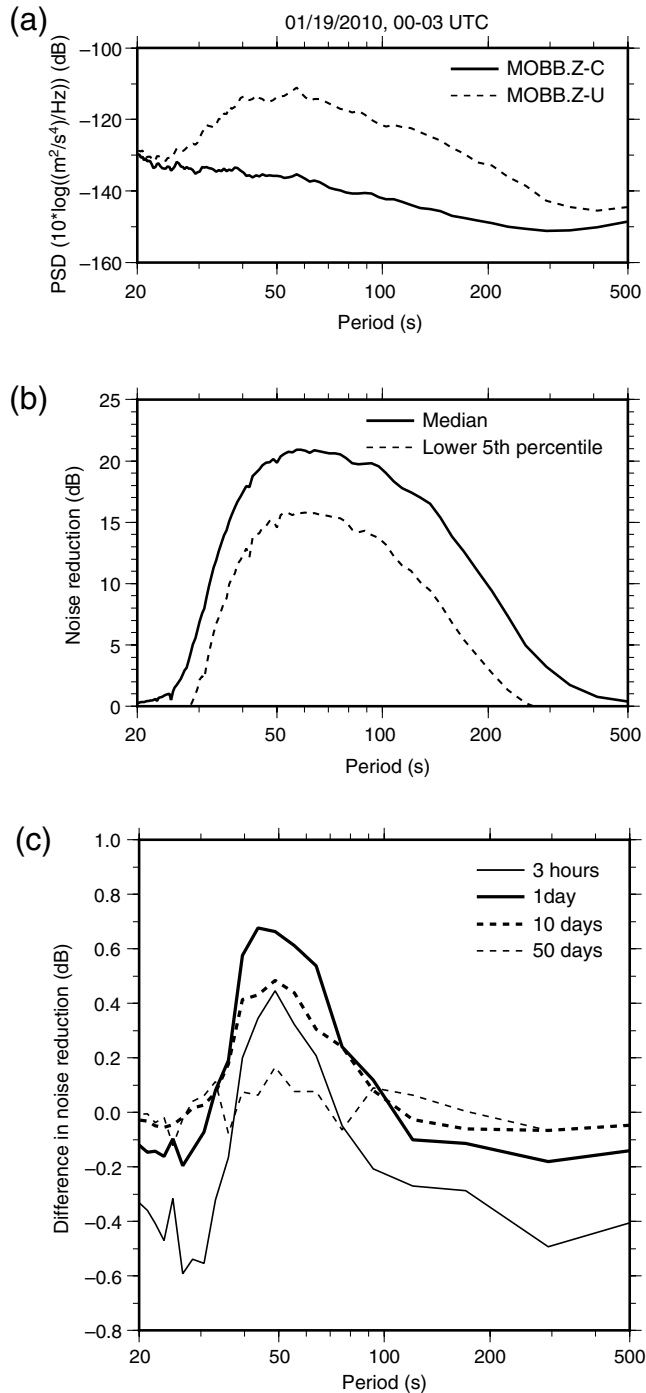


**Figure 7.** Noise removal of IG-wave-induced signals. (a) Example of the noise reduction with the reference transfer function. The solid and dashed lines are PSDs for the corrected (MOBB.Z-C) and uncorrected (MOBB.Z-U) MOBB vertical-component data, respectively. (b) The median noise reduction (the solid line) and the lower fifth percentile (the dashed line) of the noise reduction inferred from the distribution of the noise reduction distribution estimated by analyzing 4487 3 hour long records. (c) Comparison of amounts of noise reductions by different transfer functions. The four different transfer functions with time windows of 3 hours (the thin line), 1 day (the solid line), 10 days (the dashed line), and 50 days (the thin dashed line) were used to estimate the difference in median noise reduction with respect to that obtained with the reference transfer function (the solid line shown in Fig. 7b).

functions were obtained from the data collected prior to the 3 hour long segment in which we applied the transfer function. For example, in the case of the 10 day transfer function, we computed the median transfer function by stacking transfer functions obtained from data segments collected in the last 1–10 days before the 3 hour long data analyzed.

As with the estimate in the median noise reduction for the reference transfer function, we systematically analyzed our entire data set by applying four different transfer functions and obtained the median noise reduction for individual four different transfer functions. We then calculated the difference in noise reduction with respect to that obtained with the reference transfer function (Fig. 7c). Our results show that the one-day stack of transfer function obtained immediately prior to the 3 hour long data minimizes noise induced by IG waves. The improvement of noise reduction is however not more than 0.7 dB in the period range 50–100 s.

As the dominant period of IG-wave-induced signals observed at station MOBB falls in the 50–100 s period band (Fig. 2), our result shows that the reference transfer function derived from observations over a duration of several months to a year can allow us to effectively correct for the effect of IG waves on the MOBB vertical-component records without continuously calibrating the transfer function, which in turn leads to an automatic implementation of the procedure. At shorter periods (30–50 s), the reference transfer function reduces the noise level by 5–15 dB. This noise reduction however improves signal-to-noise ratios for seismic signals from local earthquakes. It is thus possible to establish rapid data processing to provide OBS data recorded at station MOBB with enhanced signal-to-noise level and, in particular, to implement it for near-real-time moment tensor analysis.

With these reference transfer functions, we minimized IG-wave-induced signals in the vertical component and estimated the background noise level of the corrected MOBB vertical-component data (MOBB.Z-C). We then compared it with that of the uncorrected MOBB Z-component data (MOBB.Z-U). The background noise level was identified as the median power spectral density (PSD) from the distributions of PSDs obtained from 3 hour long data (Fig. 8). Although the amplitude of IG-wave-induced signals varies with time, the resultant background noise level of MOBB.Z-C is about 20 dB quieter than that of MOBB.Z-U in the period band 50–100 s. The noise removal method used in this study provides an improved waveform data set on the MOBB vertical component, with reduced noise in the IG waveband.

As the variability of the one-day stack of transfer function exceeds ±2%–3% in the period band 50–100 s (Fig. 6), we need to check that the noise removal method with the reference transfer function does not remove seismic signals that are not related to the IG wave from the vertical-component data, which would introduce distortion of the resulting waveforms used for the moment tensor analysis. To investigate this issue, we applied an optimal one-day stack of transfer function for the waveforms from the local events listed in Table 1 and
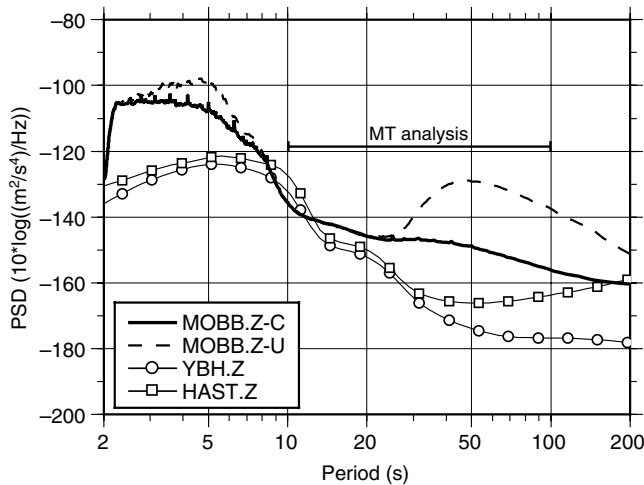
**Figure 8.** Reduction of noise level at IG wave periods (20–200 s) obtained by applying the noise removal method (equation 4). Comparison of the noise levels of the corrected (MOBB.Z-C) and uncorrected (MOBB.Z-U) MOBB vertical-component data. Also shown are the median PSDs for land stations YBH and HAST determined from all available data collected in 2011. Data in the period range 10–100 s were used for our moment tensor analysis.

examined the waveform distortion by comparing the corrected MOBB vertical-component waveforms obtained by the one-day stack of transfer function with that from the reference transfer functions (Fig. 9).

On both the corrected MOBB vertical data, the seismic phases radiated from the local events extracted by the noise removal method appear to be nearly identical, although there are residual long-period noises on the corrected waveform using the reference transfer function (the solid line shown in Fig. 9). We conclude that the reference transfer function works well to obtain the improved vertical-component data for our moment tensor analysis.

We also explored the effect of the two reference transfer functions on MOBB.Z-C records, by applying the reference transfer function obtained from the 2009–2010 data to a set

of data including seismic signals from local earthquakes that occurred in 2011. Although the MOBB.Z-C data with the 2009–2010 reference transfer function shows a reduction of IG-wave-induced signal (the thin line shown in Fig. 10), this data still exhibits long-period noise that is not present in the MOBB.Z-C data corrected using the more appropriate 2011–2012 reference transfer function (the solid line in Fig. 10). This analysis demonstrates that it is crucial to calibrate the transfer function when DPG sensors are swapped, even though the two DPG sensors have nominally the same instrument response.

### Seismic Moment Tensor Analysis

We analyzed MOBB OBS data for 12 $M_w \geq 3.5$ local earthquakes (Table 1) that occurred in northern California during March 2009 through April 2012. We used two target areas to identify local earthquakes; (1) the region between latitude 35.50° N to 35.75° N and longitude −123.00° E to −120.50° E for $M_w \geq 4.0$ earthquakes (the solid rectangle in Fig. 1), and (2) the region between latitude 36.30° N to 37.30° N and longitude −122.50° E to −121.50° E for $M_w \geq 3.5$ earthquakes (the dashed line rectangle in Fig. 1). The first target area includes the four $M_w$ 4+ earthquakes that occurred along the Calaveras fault (EV1 and EV7), on the central San Andreas fault (EV10), and near the 2003 $M_w$ 6.5 San Simeon rupture zone (EV3). The second smaller target area focuses on the northernmost creeping segment of the San Andreas fault in the San Juan Bautista region that includes eight $M_w$ 3.5+ earthquakes.

We computed MOBB.Z-C data for the 12 local earthquakes and confirmed that our noise removal method recovers the seismic phases that were previously hidden in the IG-wave-induced signals for the 5 of 12 local earthquakes (EV1, EV3, EV9, EV7, and EV10). For example, as illustrated in Figure 11, the seismic signal at periods greater than 30 s from EV1 is below the background noise level of the uncorrected MOBB vertical-component data. At periods

Table 1
Twelve Local Earthquakes Analyzed in the Study*

| Event ID | Origin Time (yyyy/mm/dd, hh:mm:ss.ss, UTC) | Latitude (°) | Longitude (°) | Depth (km) | $M_w$ | NCSS Event-ID |
|---|---|---|---|---|---|---|
| EV1 | 2009/03/30, 17:40:29.29 | 37.27932 | −121.61906 | 8.0 | 4.3 | 40234037 |
| EV2 | 2009/04/30, 22:50:54:82 | 37.25316 | −121.63780 | 7.0 | 3.5 | 51220793 |
| EV3 | 2009/06/20, 12:32:47.98 | 35.64212 | −120.95430 | 6.0 | 4.4 | 40238431 |
| EV4 | 2009/09/06, 09:47:15.38 | 36.85402 | −121.40293 | 10.0 | 3.9 | 71271995 |
| EV5 | 2009/09/09, 18:45:52.14 | 36.90356 | −121.63114 | 5.0 | 3.6 | 71278336 |
| EV6 | 2009/11/01, 14:55:34.21 | 36.63149 | −121.24828 | 11.0 | 3.6 | 71303390 |
| EV7 | 2010/01/07, 18:09:35.16 | 37.47645 | −121.79864 | 11.0 | 4.1 | 71336726 |
| EV8 | 2010/02/08, 19:56:23.88 | 36.72087 | −121.36768 | 3.0 | 3.5 | 71350686 |
| EV9 | 2011/07/06, 07:18:52.41 | 36.66374 | −121.29158 | 8.0 | 3.8 | 71596420 |
| EV10 | 2011/08/27, 07:18:21.25 | 36.58266 | −121.18108 | 8.0 | 4.6 | 71627835 |
| EV11 | 2011/08/27, 07:22:00.11 | 36.60092 | −121.20477 | 7.0 | 3.6 | 71627850 |
| EV12 | 2012/04/06, 03:16:20.02 | 36.55532 | −121.12052 | 6.0 | 3.7 | 71759475 |

*Earthquake origin times and epicentral parameters from Waldhauser and Schaff (2008; see Data and Resources) while focal depths and seismic moment magnitudes ($M_w$) determined in our moment tensor analysis. Also listed are the Northern California Seismic System (NCSS) event ID.
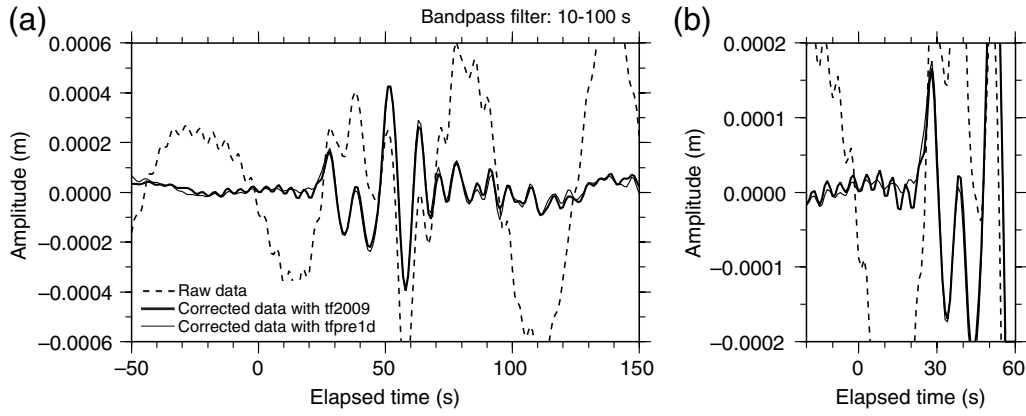
**Figure 9.**   Seismic waveforms for the EV3 $M_w$ 4.4 local earthquake. The solid and thin traces are MOBB vertical-component data after removal of the coherent DPG record by using the reference transfer function (tf2009) and the one-day stack of transfer function (tfpre1d), respectively. Also shown is the uncorrected MOBB vertical seismogram (the dashed line). A 10–100 s band-pass filter was applied to waveform data. (a) Shows 200 s long records, and (b) shows an enlarged view to illustrate residual long-period noises on the corrected waveform using the reference transfer function.
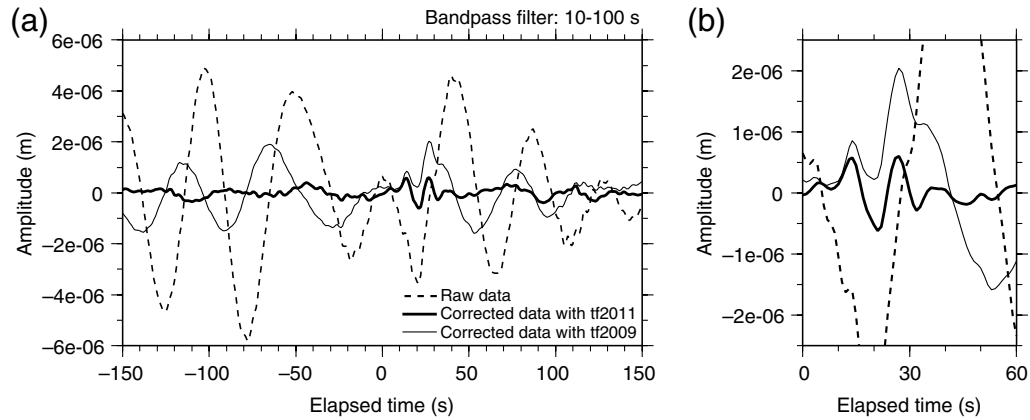


**Figure 10.**   Seismic waveforms for the EV9 $M_w$ 3.8 local earthquake. The solid trace is MOBB vertical-component data after removal of the coherent DPG record by using the reference transfer function (tf2011) obtained from the 2011–2012 MOBB data. The dashed trace is the uncorrected MOBB vertical seismogram. A 10–100 s band-pass filter was applied to waveform data. (a) Shows 3 minute long records including pre-event data, and (b) shows an enlarged view of seismic phases from the local earthquake for the time interval between 0 and 60 s from the earthquake origin time. Also shown is the corrected MOBB vertical-component data (the thin line) with the reference transfer function (tf2009) obtained from the 2009–2010 MOBB data.

shorter than 50 s, the PSD of the seismic signal exceeds the noise level of the corrected MOBB vertical-component data. The resultant PSD also appears to be above the low-noise model of the corrected MOBB vertical-component data defined as the lower fifth percentile of the PSD distribution for the corrected MOBB vertical-component data.

   Regarding the remaining seven earthquakes, there are no seismic signals obtained on MOBB.Z-C data. We thus examined expected seismic signal levels by computing the data with synthetic seismograms obtained using the seismic moment tensor solutions determined by the Northern California Seismic System (NCSS). To compute Green's functions, we used the frequency–wavenumber code of Herrmann (2009; see Data and Resources), with a one-dimensional model called GIL7 (Table 2) that is currently used for the moment tensor analysis of northern California earthquakes (Dreger

and Romanowicz, 1994). The amplitudes of the resultant expected seismic signals from these seven earthquakes are below both the background noise level and the low-noise model for MOBB.Z-C in the period range 10–100 s (Fig. 11).

   We performed the moment tensor inversion for the five local earthquakes for which we recovered seismic signals on MOBB.Z-C data (Figs. 12 and 13), assuming a double-couple source model (e.g., Stich *et al.*, 2003; Minson and Dreger, 2008; Zahradník and Custódio, 2012). The moment tensor solutions were determined with a grid search approach, by maximum variance reduction (VR):

$$VR = \left\{ 1 - \frac{\int [d_o(t) - d_s(t)]^2 \, dt}{\int [d_o(t)]^2 \, dt} \right\} \times 100, \qquad (5)$$

in which $d_o(t)$ and $d_s(t)$ are the observed and synthetic data, respectively. The grid intervals are 5° in strike, dip, and rake,
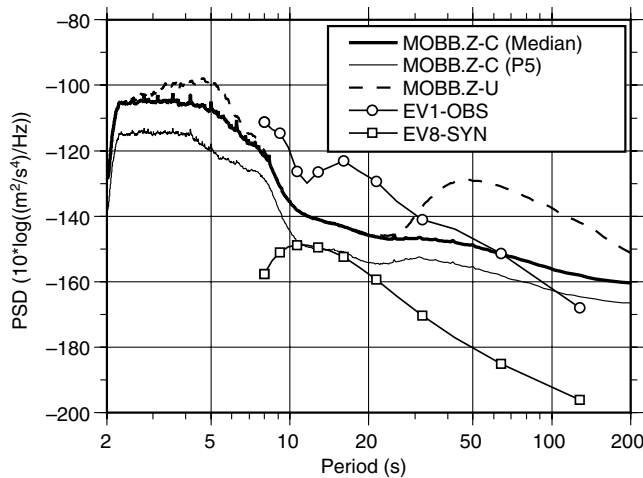
**Figure 11.**    PSDs of the corrected MOBB vertical-component data for the EV1 $M_w$ 4.3 local earthquake and the synthetic MOBB data for the EV8 $M_w$ 3.5 local earthquake. Also shown are background noise levels for the corrected (the solid line, MOBB.Z-C) and uncorrected (the dashed line, MOBB.Z-U) MOBB vertical-component data. The thin line is the low-noise model for the corrected MOBB vertical-component data based on the lower fifth percentile (P5) inferred from the distribution of the PSDs of the corrected MOBB vertical-component data.

1 km in depth, and 0.1 in $M_w$. We exclude MOBB horizontal data from the moment tensor inversion to focus on the waveform fits (or VR) for the MOBB vertical-component data.

The noise removal method significantly improves VRs in the MOBB vertical-component data for all five local earthquakes analyzed (Table 3). For example, the VR is increased from 9.2% to 63.2% for EV1 after the noise removal method is applied (Fig. 12).

We evaluated total waveform VRs for three different data sets: (1) land-station data, (2) land station with MOBB.Z-C data, and (3) land station with MOBB.Z-U data (i.e., uncorrected data). The resultant VRs obtained using both land stations and MOBB.Z-C data is comparable to those obtained using only land-station data (Fig. 14 and Table 3). Our result demonstrates the effectiveness of the noise removal method

### Table 2
One-Dimensional Velocity, Density, and Attenuation Models for Computing Green's Function*

| Thickness (km) | $V_P$ (km/s) | $V_S$ (km/s) | Density (kg/m³) | $Q_P$ | $Q_S$ |
|---|---|---|---|---|---|
| 1.0 | 3.20 | 1.50 | 2280 | 600 | 300 |
| 2.0 | 4.50 | 2.40 | 2280 | 600 | 300 |
| 1.0 | 4.80 | 2.78 | 2580 | 600 | 300 |
| 1.0 | 5.51 | 3.18 | 2580 | 600 | 300 |
| 12.0 | 6.21 | 3.40 | 2680 | 600 | 300 |
| 8.0 | 6.89 | 3.98 | 3000 | 600 | 300 |
| — | 7.83 | 4.52 | 3260 | 600 | 300 |

*One-dimensional seismic velocities for $P$ wave ($V_P$) and $S$ wave ($V_S$), as well as density from GIL7 model in Dreger and Romanowicz (1994). Seismic-attenuation parameters for $P$ wave ($Q_P$) and $S$ wave ($Q_S$) were assumed to be 600 and 300, respectively.

using the reference transfer functions to include MOBB vertical-component data in the moment tensor analysis. While the examples shown are for earthquakes that are already well constrained using the land-based network, we expect that inclusion of MOBB OBS data will be important for events that may occur offshore in the future.

As shown in Figures 12 and 13, MOBB horizontal-component data exhibit long-period noise likely induced by the effects of seafloor tilts which are strongly influenced by tides and ocean currents and are directional (Crawford and Webb, 2000; Dahm *et al.*, 2006; Dolenc *et al.*, 2008). Ocean-bottom current data from station MOBB will be used in a forthcoming study to explore the possibility of noise reductions on the horizontal components. Further assessment of noise on the horizontal components will likely require the availability of arrays of geophysical instruments, such as DPGs and ocean-bottom current meters.

### Summary and Conclusions

We have analyzed several years of continuous vertical-component MOBB broadband seismic data and DPG records and have shown that there is a strong correlation between the water pressure and the vertical component of seafloor ground velocity in the period range 30–200 s, By making use of this temporal correlation, a transfer function was determined and utilized to successfully deconvolve the IG-wave-induced signals from the vertical component of MOBB broadband data.

The maximum noise reduction (up to 20 dB) in the IG waveband is obtained by using a one-day stack of transfer function inferred from data segment collected prior to data in which the noise removal method is applied. A one-year stack of transfer function also reduces the noise level by 20 dB in the period range 50–100 s, and up to 15 dB in the period range 30–50 s. This period range is critical for regional moment tensor studies. Our result implies that we can use a median transfer function inferred from data collected for over a year to effectively correct for the effect of IG waves on the MOBB vertical-component data, without having to calibrate the transfer function each time, providing a means to obtain improved MOBB vertical-component data with reduced IG-wave-induced noise, in quasi-real-time.

The effectiveness of the noise removal method with the transfer function is demonstrated by recovering seismic phases that were previously masked by the IG-wave-induced signals for five $M_w \geq 3.5$ local earthquakes. After applying the noise removal method, the waveform fit between the observed and synthetic for the MOBB vertical-component data is significantly improved. The corrected MOBB data are then useful to determine the moment tensors of these five local earthquakes. We have implemented the IG-wave-induced signal removal method into the NCSS to enhance the real-time earthquake monitoring capability in northern California. The noise removal method developed here can also be applied to other broadband deployments on the ocean floor, as long as DPGs are installed in the vicinity of the seismic sensors.
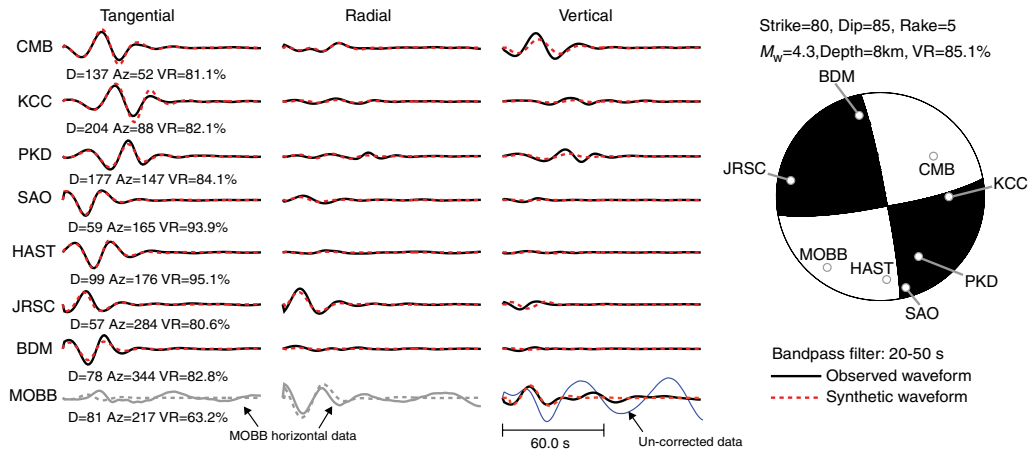
**Figure 12.** Moment tensor analysis for the EV1 $M_w$ 4.3 local earthquake. Comparison of observed and synthetic waveforms. Also shown are earthquake-station distances (*D*) in km, azimuths (Az) in degrees from north, and variance reduction (VR, equation 5). The VR for MOBB data is computed from the waveform fits of the vertical-component data only. The uncorrected MOBB vertical-component waveform is shown to illustrate the effectiveness of the noise removal method for IG-wave-induced signals. Note that MOBB horizontal-component data were not used for the moment tensor inversion, although they are shown in this figure. The color version of this figure is available only in the electronic edition.
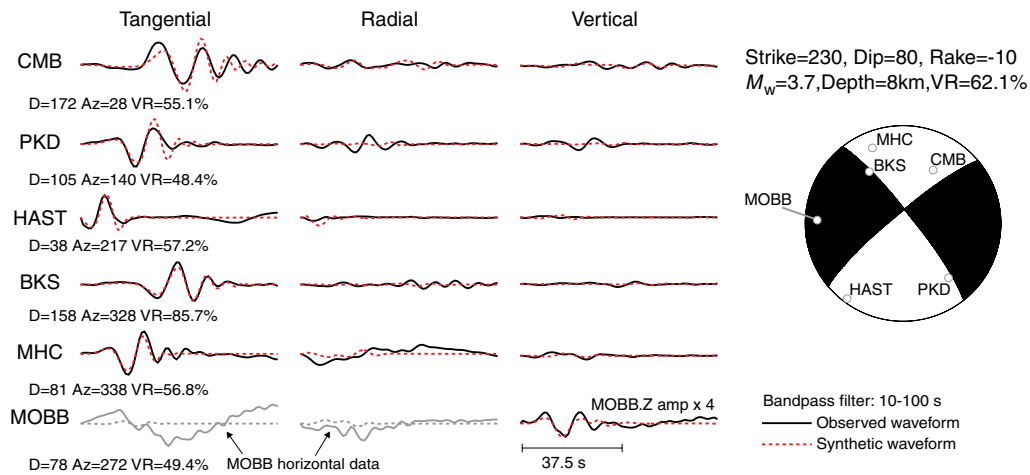


**Figure 13.** Same as Figure 12 except for the moment tensor analysis of the EV9 $M_w$ 3.8 local earthquake. The color version of this figure is available only in the electronic edition.

Table 3

Variance Reduction (VR) for Double-Couple Source Model with Different Data Sets*

| | MOBB.Z Waveform VR | | Total Waveform VR | | |
|---|---|---|---|---|---|
| Event ID | MOBB.Z-C | MOBB.Z-U | LAND | LAND+MOBB.Z-C | LAND+MOBB.Z-U |
| EV1 | 63.2 | 9.2 | 85.4 | 85.1 | 74.5 |
| EV3 | 87.6 | −5.5 | 80.7 | 81.0 | 50.6 |
| EV9 | 49.4 | 2.7 | 62.3 | 62.1 | 22.8 |
| EV7 | 73.2 | −3.5 | 80.5 | 80.3 | 45.3 |
| EV10 | 87.3 | 75.5 | 83.0 | 83.0 | 82.7 |

*MOBB.Z waveform VR shows the VR for the corrected (MOBB.Z-C) and uncorrected (MOBB.Z-U) MOBB vertical-component data for the five local events (EV1, EV3, EV9, EV7, and EV10). Total waveform VR shows three different data sets: (1) land station data (LAND), (2) land station with MOBB.Z-C data (LAND+MOBB.Z-C), and (3) land station with MOBB.Z-U data (LAND +MOBB.Z-U).
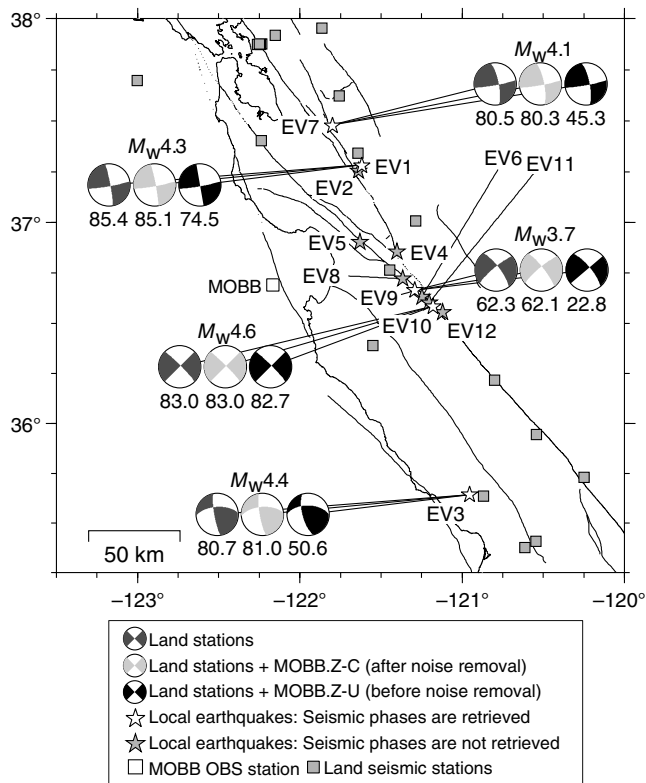
**Figure 14.** Summary plot of the moment tensor analysis for the five local earthquakes. Three moment tensor solutions are obtained for each local earthquake with different data sets. The number below each moment tensor mechanism is the total waveform VR as listed in Table 3.

## Data and Resources

Seismic data from land-based and MOBB OBS stations used in this study can be obtained from the Northern California Earthquake Data Center (quake.geo.berkeley.edu). The relocated earthquake locations were extracted from the double-difference earthquake catalog (www.ldeo.columbia.edu/~felixw/NCAeqDD and ddrt.ldeo.columbia.edu/DDRT/index.html). The surface traces of active fault were downloaded from the U.S. Geological survey Quaternary Fault and Fold Database of the United States (earthquake.usgs.gov/hazards/qfaults). Green functions used in this study were computed using the Computer Programs in Seismology package (www.eas.slu.edu/eqc/eqccps.html; Herrmann, 2009). Some plots are made using the Generic Mapping Tools version 4.1 (www.soest.hawaii.edu/gmt; Wessel and Smith, 1998). Some data analyses were completed using the Seismic Analysis Code (www.iris.edu/software/sac; Goldstein and Snoke, 2005). All websites were last accessed January 2013.

## Acknowledgments

## References

Araki, E., M. Shinohara, S. Sacks, A. Linde, T. Kanazawa, H. Shiobara, H. Mikada, and K. Suyehiro (2004). Improvement of seismic observation in the ocean by use of seafloor boreholes, *Bull. Seismol. Soc. Am.* **94,** 678–690, doi: 10.1785/0120020088.

Baba, T., K. Hirata, and Y. Kaneda (2004). Tsunami magnitudes determined from ocean-bottom pressure gauge data around Japan, *Geophys. Res. Lett.* **31,** L08303, doi: 10.1029/2003GL019397.

Barzilai, A., T. VanZandt, and T. Kenny (1998). Technique for measurement of the noise of a sensor in the presence of large background signals, *Rev. Sci. Instrum.* **69,** 2767–2772.

Bécel, A., M. Laigle, J. Diaz, J.-P. Montagner, and A. Hirn (2011). Earth's free oscillations recorded by free-fall OBS ocean-bottom seismometers at the Lesser Antilles subduction zone, *Geophys. Res. Lett.* **38,** L24305, doi: 10.1029/2011GL049533.

Bendat, J. S., and A. G. Piersol (1986). *Random Data: Analysis and Measurement Procedures,* John Wiley and Sons, New York, 566 pp.

Bernardi, F., J. Braunmiller, U. Kradolfer, and D. Giardini (2004). Automatic regional moment tensor inversion in the European-Mediterranean region, *Geophys. J. Int.* **157,** 703–716.

Brandt, M. B. C., and I. Saunders (2011). New regional moment tensors in South Africa, *Seismol. Res. Lett.* **82,** no. 1, 69–80.

Bromirski, P. D., O. V. Sergienko, and D. R. MacAyeal (2010). Transoceanic infragravity waves impacting Antarctic ice shelves, *Geophys. Res. Lett.* **37,** L02502, doi: 10.1029/2009GL041488.

Clinton, J. F., E. Hauksson, and K. Solanki (2006). An evaluation of the SCSN moment tensor solutions: Robustness of the $M_w$ magnitude scale, style of faulting and automation of the method, *Bull. Seismol. Soc. Am.* **96,** no. 5, 1689–1705, doi: 10.1785/0120050241.

Cox, C., T. Deaton, and S. Webb (1984). A deep-sea differential pressure gauge, *J. Atmos. Oceanic Technol.* **1,** 237–246.

Crawford, W. C., and S. C. Webb (2000). Identifying and removing tilt noise from low-frequency ($< 0.1$ Hz) seafloor vertical seismic data, *Bull. Seismol. Soc. Am.* **90,** no. 4, 952–963, doi: 10.1785/0119990121.

Crawford, W. C., R. A. Stephen, and S. T. Bolmer (2006). A second look at low-frequency marine vertical seismometer data quality at the OSN-1 site off Hawaii for seafloor, buried, and borehole emplacements, *Bull. Seismol. Soc. Am.* **96,** no. 5, 1952–1960.

Dahm, T., F. Tillmann, and J. P. Morgan (2006). Seismic broadband ocean-bottom data and noise observed with free-fall stations: Experiences from long-term deployments in the North Atlantic and the Tyrrhenian Sea, *Bull. Seismol. Soc. Am.* **96,** 647–664, doi: 10.1785/0120040064.

Dolenc, D., B. Romanowicz, P. McGill, and W. Wilcock (2008). Observations of infragravity waves at the ocean-bottom broadband seismic stations Endeavour (KEBB) and Explorer (KXBB), *Geochem. Geophys. Geosys.* **9,** Q05007, doi: 10.1029/2008GC001942.

Dolenc, D., B. Romanowicz, D. Stakes, P. McGill, and D. Neuhauser (2005). Observations of infragravity waves at the Monterey ocean bottom broadband station (MOBB), *Geochem. Geophys. Geosys.* **6,** Q09002, doi: 10.1029/2005GC000988.

Dolenc, D., B. Romanowicz, R. Uhrhammer, P. McGill, D. Neuhauser, and D. Stakes (2007). Identifying and removing noise from the Monterey ocean bottom broadband seismic station (MOBB) data, *Geochem. Geophys. Geosys.* **8,** Q02005, doi: 10.1029/2006GC001403.

Dreger, D., and D. Helmberger (1991). Source parameters of the Sierra Madre Earthquake from regional and local body waves, *Geophys. Res. Lett.* **18,** no. 11, 2015–2018, doi: 10.1029/91GL02366.

Dreger, D., and B. Romanowicz (1994). Source characteristics of events in the San Francisco Bay Region, *U.S. Geol. Surv. Open-File Rept. 94-176*, 301–309.

Ford, S. R., D. S. Dreger, and W. R. Walter (2010). Network sensitivity solutions for regional moment tensor inversions, *Bull. Seismol. Soc. Am.* **100**, 1962–1970.

Goldstein, P., and A. Snoke (2005). "SAC availability for the IRIS community", Incorporated Institutions for Seismology Data Management Center Electronic Newsletter, available online at: http://www.iris.edu/dms/newsletter/vol7/no1/ (last accessed January 2013).

Guilhem, A., and D. S. Dreger (2011). Rapid detection and characterization of large earthquakes using quasi-finite-source Green's functions in continuous moment tensor inversion, *Geophys. Res. Lett.* **38**, L13318, doi: 10.1029/2011GL047550.

Herbers, T. H. C., S. Elgar, and R. T. Guza (1995). Generation and propagation of infragravity waves, *J. Geophys. Res.* **100**, 24,863–24,872.

Herrmann, R. B. (2009). Computer programs in seismology, version 3.30, http://www.eas.slu.edu/eqc/eqccps.html (last accessed January 2013).

Ichinose, G. A., J. G. Anderson, K. D. Smith, and Y. Zeng (2003). Source parameters of eastern California and western Nevada earthquakes from regional moment tensor inversion, *Bull. Seismol. Soc. Am.* **93**, 61–84.

Ito, Y., T. Tsuji, Y. Osada, M. Kido, D. Inazu, Y. Hayashi, H. Tsushima, R. Hino, and H. Fujimoto (2011). Frontal wedge deformation near the source region of the 2011 Tohoku-Oki earthquake, *Geophys. Res. Lett.* **38**, L00G05, doi: 10.1029/2011GL048355.

Kao, H., P. Jian, K. Ma, B. Huang, and C. Liu (1998). Moment-tensor inversion for offshore earthquakes east of Taiwan and their implications to regional collision, *Geophys. Res. Lett.* **25**, no. 19, 3619–3622.

Kubo, A., E. Fukuyama, H. Kawai, and K. Nonomura (2002). NIED seismic moment tensor catalogue for regional earthquakes around Japan: Quality test and application, *Tectonophysics* **356**, 23–48, doi: 10.1016/S0040-1951(02)00375-X.

Laske, G., J. A. Collins, C. J. Wolfe, S. C. Solomon, R. S. Detrick, J. A. Orcutt, D. Bercovici, and E. H. Hauri (2009). Probing the Hawaiian hot spot with new Broadband Ocean Bottom instruments, *Eos Trans. AGU* **90**, no. 41, 362–363, doi: 10.1029/2009EO410002.

Maeda, T., T. Furumura, S. Sakai, and M. Shinohara (2011). Significant tsunami observed at the ocean-bottom pressure gauges at 2011 off the Pacific coast of Tohoku earthquake, *Earth Planets Space* **63**, 803–808, doi: 10.5047/eps.2011.06.005.

Minson, S., and D. Dreger (2008). Stable inversions for complete moment tensors, *Geophys. J. Int.* **174**, 585–592, doi: 10.1111/j.1365-246X.2008.03797.x.

Munk, W. H. (1949). Surf beats, *Eos Trans. AGU* **30**, 849–854.

Obrebski, M., R. M. Allen, F. Pollitz, and S.-H. Hung (2011). Lithosphere-asthenosphere interaction beneath the western United States from the joint inversion of body-wave traveltimes and surface-wave phase velocities, *Geophys. J. Int.* **185**, 1003–1021, doi: 10.1111/j.1365-246X.2011.04990.x.

Pasyanos, M. E. (2005). A variable resolution surface wave dispersion study of Eurasia, North Africa and surrounding regions, *J. Geophys. Res.* **110**, B12301.

Pasyanos, M. E., D. S. Dreger, and B. Romanowicz (1996). Toward real-time estimation of regional moment tensors, *Bull. Seismol. Soc. Am.* **86**, no. 5, 1255–1269.

Peterson, J. (1993). Observation and modeling of seismic background noise, *U.S. Geol. Surv. Tech. Rept. 93-322*, 95 pp.

Ritzwoller, M. H., N. M. Shapiro, M. P. Barmin, and A. L. Levshin (2002). Global surface wave diffraction tomography, *J. Geophys. Res.* **107**, no. B12, 2335, doi: 10.1029/2002JB001777.

Romanowicz, B., D. Dreger, M. Pasyanos, and R. Uhrhammer (1993). Monitoring of strain release in central and northern California using broadband data, *Geophys. Res. Lett.* **20**, 1643–1646.

Romanowicz, B., P. McGill, D. Neuhauser, and D. Dolenc (2009). Acquiring real time data from the broadband ocean bottom seismic observatory at Monterey Bay (MOBB), *Seismol. Res. Lett.* **80**, no. 2, 197–202.

Romanowicz, B., D. Stakes, D. Dolenc, D. Neuhauser, P. McGill, R. Uhrhammer, and T. Ramirez (2006). The Monterey Bay broadband ocean bottom seismic observatory, *Ann. Geophys.* **49**, 607–623.

Romanowicz, B., D. Stakes, R. Uhrhammer, P. McGill, D. Neuhauser, T. Ramirez, and D. Dolenc (2003). The MOBB experiment: A prototype permanent off-shore ocean bottom broadband station, *Eos Trans. AGU* **84**, no. 34, 325.

Saito, T., Y. Ito, D. Inazu, and R. Hino (2011). Tsunami source of the 2011 Tohoku-Oki earthquake, Japan: Inversion analysis based on dispersive tsunami simulations, *Geophys. Res. Lett.* **38**, L00G19, doi: 10.1029/2011GL049089.

Saito, T., T. Matsuzawa, K. Obara, and T. Baba (2010). Dispersive tsunamis of the 2010 Chile earthquake recorded by the high-sampling-rate ocean-bottom pressure gauges, *Geophys. Res. Lett.* **37**, L23303, doi: 10.1029/2010GL045290.

Sipkin, S. A. (1982). Estimation of earthquake source parameters by the inversion of waveform data: Synthetic waveforms, *Phys. Earth Planet. In.* **30**, no. 2, 242–259.

Snodgrass, F. E., G. W. Groves, K. F. Hasselmann, G. R. Miller, W. H. Munk, and W. H. Powers (1966). Propagation of ocean swell across the Pacific, *Phil. Trans. Roy. Soc. Lond. A* **259**, no. 1103, 431–497.

Stich, D., C. J. Ammon, and J. Morales (2003). Moment tensor solutions for small and moderate earthquakes in the Ibero-Maghreb region, *J. Geophys. Res.* **108**, no. B3, 2148, doi: 10.1029/2002JB002057.

Sutton, G. H., W. G. McDonald, D. D. Prentiss, and S. N. Thanos (1965). Ocean-bottom seismic observatories, *Proc. IEEE* **53**, 1909–1921.

Tajima, F., C. Megnin, D. S. Dreger, and B. Romanowicz (2002). Feasibility of real-time broadband waveform inversion for simultaneous moment tensor and centroid location determination, *Bull. Seismol. Soc. Am.* **92**, 739–750.

Tucker, M. J. (1950). Surf beats: Sea waves of 1 to 5 min. period, *Proc. R. Soc. A* **202**, 565–573.

Waldhauser, F., and D. P. Schaff (2008). Large-scale relocation of two decades of Northern California seismicity using cross-correlation and double-difference methods, *J. Geophys. Res.* **113**, no. B08311, doi: 10.1029/2007JB005479.

Webb, S. C. (1998). Broadband seismology and noise under the ocean, *Rev. Geophys.* **36**, no. 1, 105–142, doi: 10.1029/97RG02287.

Webb, S. C., and W. C. Crawford (1999). Long period seafloor seismology and deformation under ocean waves, *Bull. Seismol. Soc. Am.* **89**, 1535–1542.

Webb, S. C., and W. C. Crawford (2010). Shallow-water broadband OBS seismology, *Bull. Seismol. Soc. Am.* **100**, no. 4, 1770–1778, doi: 10.1785/0120090203.

Webb, S., X. Zhang, and W. Crawford (1991). Infragravity waves in the deep ocean, *J. Geophys. Res.* **96**, no. C2, 2723–2736, doi: 10.1029/90JC02212.

Wessel, P., and W. H. F. Smith (1998). New, improved version of the Generic Mapping Tools released, *EOS Trans. AGU* **79**, 329.

Yang, Z., A. F. Sheehan, J. A. Collins, and G. Laske (2012). The character of seafloor ambient noise recorded offshore New Zealand: Results from the MOANA ocean bottom seismic experiment, *Geochem. Geophys. Geosys.* **13**, Q10011, doi: 10.1029/2012GC004201.

Zahradník, J., and S. Custódio (2012). Moment tensor resolvability: Application to southwest Iberia, *Bull. Seismol. Soc. Am.* **102**, 1235–1254, doi: 10.1785/0120110216.

Berkeley Seismological Laboratory
University of California, Berkeley
215 McCone Hall
Berkeley, California 94706